Enhanced Photocatalytic Oxygen Evolution by Crystal Cutting

Min Sun, Shijie Xiong, Xinglong Wu, Chengyu He, Tinghui Li, and Paul K. Chu**

Photocatalytic water splitting by solar power is environmentally friendly and highly preferred.[1] The oxygen evolution reaction (OER) is key to renewable-energy technologies such as rechargeable metal-air batteries[2–4] and water splitting,[5,6] and water oxidation also plays an important role in energy storage such as solar fuel synthesis.[7,8] Despite extensive research, the effects of a catalytic surface on the OER are still not well understood[9] and the development of economical oxygen electrode catalysts with high activity under visible-light irradiation remains a great challenge. Recently, Yang[10] proposed that crystal cutting might increase the photocatalytic properties of materials such as Cu_2O nanocrystals.[11,12] Although Cu_2O delivers good performance in the photodegradation of methyl orange after crystal cutting,[12] there has been no report on the direct photocatalytic water splitting into hydrogen or oxygen. In fact, surface oxidation of Cu_2O to CuO introduces unstable photocatalytic characteristics in aqueous solutions after long-time irradiation.[13] Markovic and co-workers reported enhanced hydrogen evolution from water splitting by tailoring the $Li^+(Ni(OH)_2(Pt$ interfaces,[14] but enhancement by crystal tailoring has not been reported. In this respect, it is crucial to develop crystal-cut photocatalytic materials with excellent oxygen evolution ability under visible-light irradiation and to elucidate the associated mechanism.

In_2O_3 is a promising semiconducting material[15–17] and has a bandgap of 2.8 eV. However, it has poor photocatalytic properties[18] and no water splitting has been reported experimentally using In_2O_3 octahedron nanocrystals, although there has been litle theoretical work on water splitting on some special crystal facets.[19] Here, we report a simple technique to produce uniformly cut In_2O_3 truncated octahedrons. Our theoretical analysis shows that the {100} facet on the In_2O_3 truncated octahedrons enhances oxygen evolution in photocatalysis and photoelectrochemical measurements provide the experimental evidence.

In a body-center-cube (bcc) structural crystal such as Cu_2O, the difference in the energy levels between the crystal faces can drive the photoexcited electrons and holes to different crystal faces, leading to the separation of electrons and holes. Previous investigation suggests that during irradiation by visible light, the photogenerated holes on the {111} facets will transfer to the {100} facets, whereas electrons on the {100} facets will migrate to the {111} facets.[20] This is a prerequisite to the water-splitting reaction.[7] The catalytic activity on the {111} facets stems from the Cu-terminated surfaces bonded with some stable groups.[21] Hence, the electrically neutral {100} facets cannot interact well with charged molecules and is thus catalytically inactive.[22] This implies that polar facets on the In_2O_3 crystal having the same crystal structure and adequate bandgap[23,24] as Cu_2O may increase the photocatalytic activity in the water-splitting reaction.

Figure 1a depicts the In_2O_3 octahedron[24,25] and Figure 1b–d show the atomic arrangements in a unit cell of the bcc structure along different lattice directions. The smaller and bigger spheres represent oxygen and indium atoms, respectively. The (002), (020), and (200) facets are arranged by the same type of atoms (indium or oxygen) as shown in Figure 1b,c. The distances between two adjacent facets are the same and they are the polar facets. The (220) and (222) facets, which have two different atoms (indium and oxygen) (Figure 1c,d), show electrical neutrality and are the nonpolar facets.

The spatial distributions of electron and holes excited by light irradiation on these crystal facets are theoretically investigated and the calculation details are described in Figure S1–S3 in the Supporting Information. The main panel in Figure S4a in the Supporting Information presents the densities of states (DOSs) of the bulk and slabs along the {100} and {111} directions of In_2O_3. Compared with the bulk materials and {111} surface, cleaving of the {100} surface creates a new valence subband (represented by peak A in the DOS) which is just below but very close to the Fermi level defined as the energy of the highest occupied state and set to zero energy. The spatial distribution of the orbital in this subband shown in the inset illustrates that the orbital is concentrated on the {100} surface. At the same time, the orbitals of the conduction band in both the {100} and {111} slabs are extended to the entire materials (see the Supporting Information). This implies that during light irradiation, the excited holes from valence sub-band A are concentrated on the {100} facets and the excited electrons are in the bulk. This produces a photoinduced dipole layer on the {100} facet, which may attract OH^- groups from the solution. Such charge separation had been observed in small TiO_2 particles based on density functional calculations.[26] To investigate the effects of the {100} facets on H_2O molecules, we perform geometry optimization on the {111} and {100} slabs with adsorbed H_2O molecules. The optimized structures are shown in Figure S4b in the Supporting Information. On the {100} surfaces with

M. Sun, Prof. S. J. Xiong, Prof. X. L. Wu,
Dr. C. Y. He, Dr. T. H. Li
National Laboratory of Solid State Microstructures
and Department of Physics
Nanjing University
Nanjing, 210093, P. R. China
E-mail: hkxlwu@nju.edu.cn
Prof. P. K. Chu
Department of Physics and Materials Science
City University of Hong Kong
Tat Chee Avenue, Kowloon, Hong Kong, China
E-mail: paul.chu@cityu.edu.hk

**ADVANCED
MATERIALS**

www.advmat.de

**Materials
Views**

www.MaterialsViews.com

COMMUNICATION
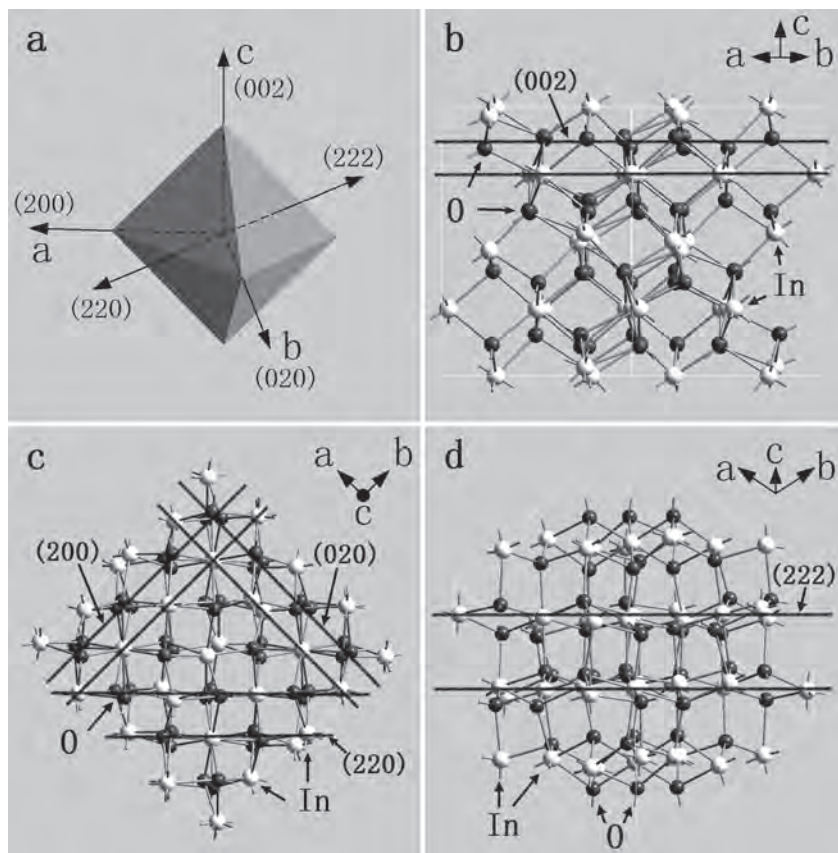
Figure 1. a) Sketch of the In_2O_3 octahedron. b) A unit cell of the bcc structure viewed from the <220> direction with the lines representing the (002) facets. c) A unit cell of the bcc structure viewed from the <002> direction with the lines representing the (200), (020), and (220) facets. d) A unit cell of the bcc structure viewed from the direction parallel to the (222) facet with the lines representing the (222) facets.

and without induced charges, there are some H_2O molecules that dissociate into H^+ and OH^-, whereas on the {111} surface, they cannot dissociate. The calculated DOS for the {100} slab with adsorbed H_2O molecules is shown in Figure S5,S6 in the Supporting Information. Although there are some changes in detailed structures compared to that without H_2O molecules, peak A which is responsible for the creation of holes still exists. Dissociation of H_2O molecules on different surfaces has been investigated based on first-principle calulation.[26–28] In this work, we perform geometry optimization for the surfaces with different H_2O monolayer coverage from 1/8 to 1/2 and observe that 1/8 coverage is related to the dissociation for 1/2 water monolayer coverage on the {100} surface. Partial dissociation on the {100} surface may stem from the complicated In and O exposed structure.

The calculation results also indicate that the {100} facets of In_2O_3 can effectively accumulate holes produced by light illumination, but on the nonpolar planes such as {222} and {220}, no corresponding process occurs. In an alkaline electrolyte, when there is an accumulation of holes (h^+) on the surface, the In_2O_3 nanocrystal anode would undergo the following reaction: $4OH^- + 4h^+_{(VB)} \rightarrow O_2\uparrow + 2H_2O$, cathode: $2H_2O + 2e^-_{(CV)} \rightarrow H_2\uparrow + 2OH^-$.[29–31] Hence, if the In_2O_3 nanocrystals with {100} facets

are used as the anode, the photoexcited holes will transfer to the {100} surfaces to produce O_2. This photo-electrochemical process will lead to effective oxygen evolution from the anode, thus providing a useful way to produce O_2 based on crystal cutting.

Since various crystal facets have different growth rates,[25] the growth temperature and time must be tightly controlled in order to prepare In_2O_3 nanocrystals with the {100} surface exposed. The commonly fabricated In_2O_3 nanocrystals have the octahedral structure with the {111} surface for minimum surface free energy, and so the {100} In_2O_3 nanocrystals should be formed in the early stage. Details regarding the In_2O_3 nanocrystal growth process and mechanism are described in Figure S7 in the Supporting Information.
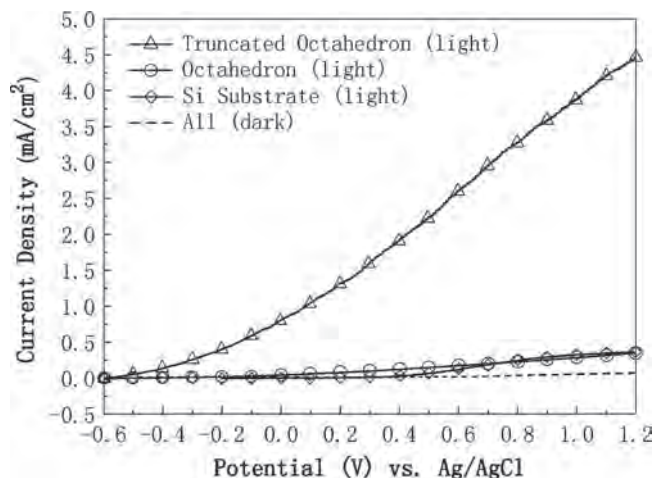
By properly controlling the growth conditions, In_2O_3 octahedrons and truncated octahedrons with a uniform size can be produced in abundance, as shown in **Figure 2**a–d. Field-emission scanning electron microscopy (FE-SEM) reveals that the size of the truncated octahedrons is about 1 μm, which is almost equal to that of the octahedrons. Field-emission transmission electron microscopy (FE-TEM) images and selected area electron diffraction (SAED) patterns are acquired to confirm the observed different crystal facets. As shown in Figure 2e–g, the hexagonal symmetry diffraction spots are obviously observed from the (111) facets on the octahedron or truncated octahedron and meanwhile, the tetragonal symmetry diffraction spots arise from the (100) facets on the truncated octahedron (Figure 2h–j). The X-ray diffraction (XRD) patterns acquired from these In_2O_3 octahedrons and truncated octahedrons are displayed in Figure 2k. All the XRD peaks can be indexed to the (200), (211), (222), (400), (411), (440), (600), and (622) reflections of the bcc structure of In_2O_3 (according to the standard card of XRD, JCPDS card No. 06-416). In particular, the (222) peak from the octahedron sample is rather strong, but that from the truncated octahedron is relatively weak. The intensity of the (400) peak from the truncated octahedrons is enhanced. Although the XRD spectra are not related to the relative areas of the various crystal faces, considering the FE-SEM and FE-TEM results, it can be inferred that a large number of {100} facets are formed. According to the UV–vis diffusive reflectance spectra of the octahedron and truncated octahedron samples, the absorption curves are acquired and Figure S8 in the Supporting Information shows that the two kinds of octahedron samples have almost the same absorption features in the visible range.

The photoelectrochemical measurements were performed in a three-electrode cell (Figure S9 in the Supporting Information) connected to a CHI 660D work station (CH Instrument) at ≈25 °C. The In_2O_3 nanocrystal sample with Ohmic contact served as the working electrode,[32,33] whereas Ag/AgCl
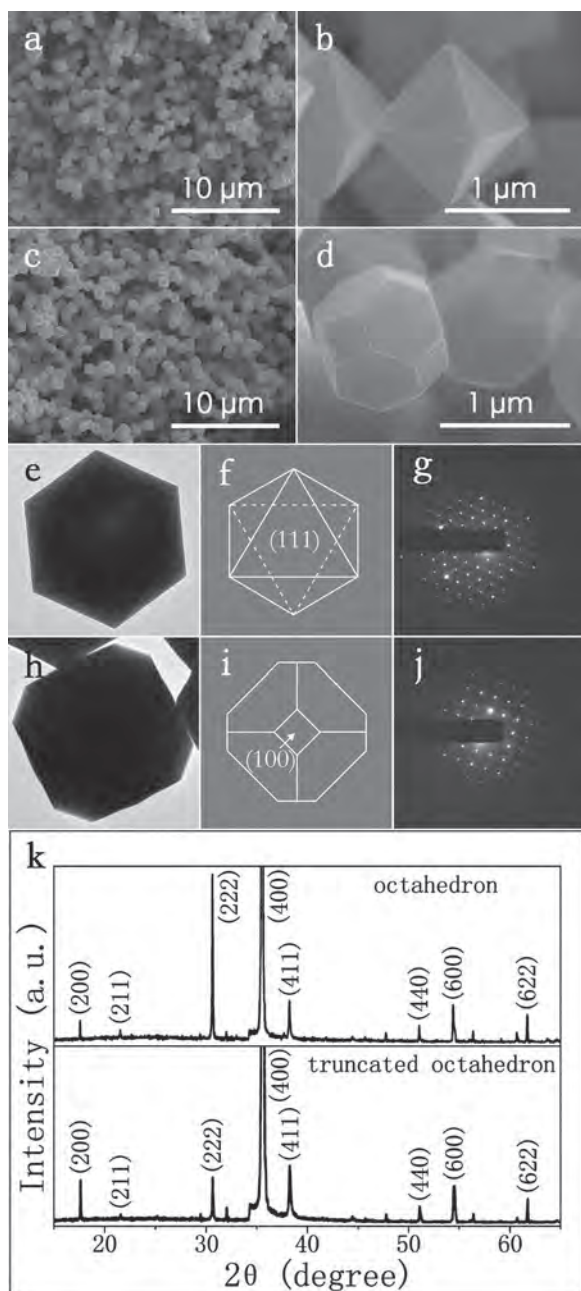
Figure 2. a) Low-magnification FE-SEM image of the octahedrons. b,c) Local enlargement (b) and low magnification (c) FE-SEM images of the truncated octahedrons. d,e) Local enlargement (d) and low-magnification (e) FE-TEM images of the octahedron. f) Sketch of octahedron viewed from the (111) facets. g) SAED pattern on the (111) facets. h) Low-magnification FE-TEM image of the octahedron. i) Sketch of the octahedron view from the (100) facets. j) SAED pattern acquired from the (100) facets. k) XRD patterns of the octahedron (upper curve) and truncated octahedron (under curve) samples.


Figure 3. Current density versus applied potential curves of photoelectrochemical measurement. The circular and triangular curves are acquired from the two In_2O_3 samples with octahedron and truncated octahedron sizes of 1 µm, respectively. The quadrate curve is from the silicon substrate. The broken line represents the cases for the octahedrons, truncated octahedrons, and silicon substrate without irradiaition (dark).

(1 mol L^{-1} NaOH-filled) and a platinum wire were the reference and counter electrodes, respectively. The current–voltage (J–V) curves are shown in **Figure 3**. The circular, triangular, and quadrate curves are acquired from two In_2O_3 samples and a silicon substrate under illumination, respectively. The broken curve

represents the cases for the octahedron, truncated octahedron, and silicon substrate samples without irradiation (dark). As the applied voltage is increased slowly from negative (–0.6 V) to positive (1.2 V), the broken curve is almost a straight line. Under Xe-lamp illumination, the photocurrent densities of both the octahedron sample and silicon substrate show little improvement compared with that without illumination, whereas that of the truncated octahedron sample (triangular curve) largely surpasses those of the octahedron sample and silicon substrate. To rule out that the rapid increase of the photocurrent density is due to different defect concentration, we mesaured the resistivity of the octahedron and truncated octahedron samples and the values are 353 and 578 mΩ cm, respectively. Hence, the truncated octahedron sample should have a smaller photocurrent, but our experimental results are not so, indicating that the {100} truncated octahedrons really have a high photocatalytic activity. Hence, the rapid increase indicates that the exposed truncated facets play an important role in the enhancement of the photocatalytic activity on the In_2O_3 nanocrystals.

To investigate the effective photocatalytic OER further, the applied voltage was fixed at 0.22 V versus Ag/AgCl and the photocatalytic current–time (I–t) curves are depicted in **Figure 4**. The triangular and circular curves are for the truncated octahedron and octahedron samples, respectively, under illumination, whereas the broken curve is acquired without illumination showing that no current is produced. During illumination, the photocurrent density measured from the octahedron sample is very small (0.04 mA cm^{-2}), but that from the truncated octahedral sample is larger (1.4 mA cm^{-2}) and remains stable during the entire observation time of 150 min. Almost no attenuation was observed, indicating both a robust and a stable photocatalytic activity. Two digital photos were taken from the truncated octahedral electrodes at 20 and 60 mins (an enlarged photo is shown in Figure S10 in the Supporting Information). In the initial stage, no bubbles were observed but as time elapsed,

COMMUNICATION
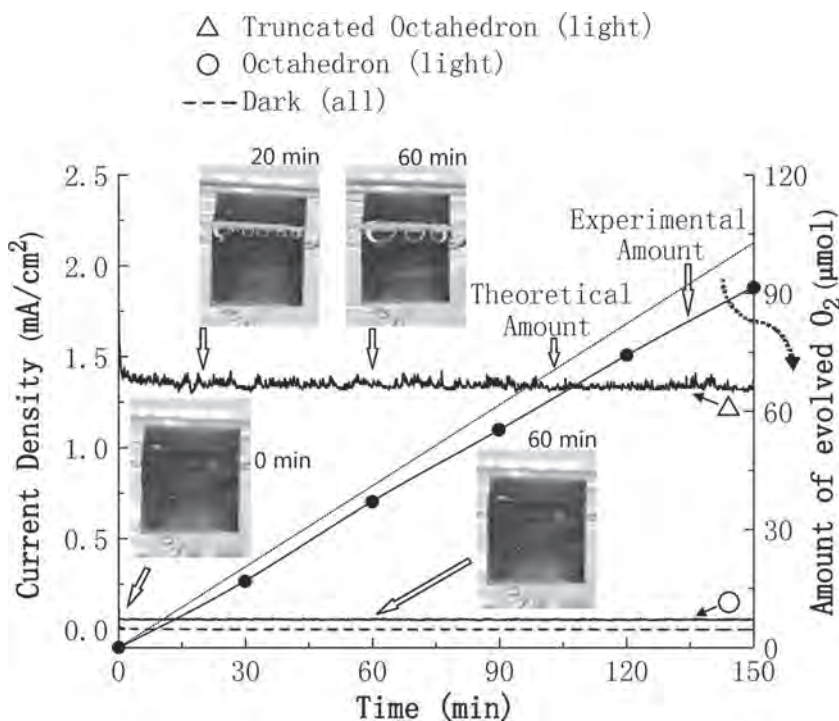
Figure 4. Current density versus time curves and two digital photos for oxygen evolution. The triangular and circular curves are for the truncated octahedron and octahedron samples under illumination, respectively, whereas the broken curve is for the case without illumination. The upper insets show representative photocatalytic-oxygen-evolution photos of the truncated octahedron sample at different measurement times taken by a digital camera from the cell at an applied potential of 0.22 V (versus Ag/AgCl). No bubbles (oxygen evolution) are observed for the octahedron sample (lower insets). Two sloping curves show the amounts of evolved O_2 calculated theoretically and detected experimentally, respectively.

bubbles were produced gradually and they became bigger and bigger. In contrast, no bubbles could be observed from the solution surface with the octahedron electrode (lower inset). The amount of evolved O_2 was calculated from the (I–t) curve and detected by a Shimadzu GC-8A gas chromatograph. The two sloping curves in Figure 4 show the theoretical and experimental results, respectively. It is obvious that the amount of evolved O_2 increases with time and the experimental value is close to the theoretical one. In addition, the SEM image and XRD spectrum after the photoelectrochemical measurement confirm that the truncated octahedrons remain intact on the electrode (Figure S11 in the Supporting Information). These above provide experimental evidence that In_2O_3 possesses good photocatalytic characteristics after crystal cutting and it is consistent with the theoretical prediction described earlier. The truncated octahedrons have the advantage of multiple (100) facets being exposed to accumulate holes via photo-excited charge-carrier separation. This is responsible for the high photocatalytic activity. Furthermore, in comparison with Cu_2O, the polar surfaces on In_2O_3 are stable in aqueous solutions and it is crucial to stable water splitting photocatalytically. Here, we would like to point out that the (100) facet is a polar surface and undergoes evident surface reconstruction in the aqueous environment (Supporting Information, Figure S4b), thereby improving the photocatalytical activity on the (100) facets further.

In conclusion, we have fabricated uniform truncated In_2O_3 nanocrystals on a large-scale on a silicon substrate using a simple technique. The experimental photocatalytic performance of the In_2O_3 truncated octahedrons is consistent with our theoretical prediction showing that the {100} truncated octahedrons have significantly improved photocatalytic activity compared with the octahedrons. The high photocurrent (1.4 mA cm^{-2}, voltage = 0.25 V vs. Ag/AgCl) and the long-time oxygen evolution without attenuation indicate that the In_2O_3 truncated octahedrons are promising for photocatalytic oxygen evolution, and our results provide evidence that crystal cutting plays an important role in photofunctionization of materials.

Experimental Section

Sample Preparation: Indium oxide (In_2O_3) nanostructures were fabricated using a standard chemical vapor deposition (CVD) instrument. Indium oxide and graphite powders were mixed to a certain percentage (mass ratio = 1.5:1), ground, placed on an prepared alumina boat, and inserted into the CVD chamber. A gas mixture containing 98% of high-purity Ar and 2% of high-purity O_2 served as the carrier gas and the pressure was maintained at 1 atm during the nanocrystal growth. A single-crystal n-type silicon wafer (<100> oriented, 0.5 mm thick, 1–10 Ω cm resistivity) was cut into smaller 8 mm × 10 mm pieces and used as the substrate. A thin layer of gold (10 nm) was predeposited on the silicon substrate by sputtering. The substrate was positioned downstream of the source and the furnace was heated from room tempearture to 1000 °C at a rate of 50 °C min^{-1} and a gas flow of 150 sccm. When the furnace temperature reached 950 °C, the truncated octahedrons were obtained and deposited for 3 h at the same gas flow of 150 sccm to obtain the corresponding sample. When the furnace was heated to 1000 °C, the octahedrons were obtained at a gas flow 100 sccm and deposited for 3 h (Supporting, Information, Figure S7). By adopting the aforementioned growth control, the thickness of the octahedron and truncated octahedron samples obtained by a Zeta 20 (Zeta Instruments, United States) was almost the same (22.7 μm) (Supporting Information, Figure S8).

Characterization: The In_2O_3 nanocrystal structures were determined by XRD (Philips, Xpert) and the nanocrystal sizes and surface morphology were examined by FE-SEM (Hitachi, S4800). The photo-electrochemical measurements were performed on a three-electrode cell connected to a CHI 660D work station (CH Instrument) at ≈25 °C. On the backside of the Si substrate, an Ohmic contact was established by embedding a coiled Cu wire in a eutectic gallium-indium alloy (Aldrich) that wetted the silicon. The Cu wire and the eutectic alloy were subsequently covered with silver paint (SPI supplies). The silver layer in contact with the Cu wire was used as working electrode and it was not immersed in the electrolyte, whereas Ag/AgCl (1 mol L^{-1} NaOH-filled) and a platinum wire served as the reference and counter electrodes, respectively. The electrolyte was a 1 mol L^{-1} NaOH solution (pH = 13.6) and a 500 W Xe lamp served as the light source in the photo-electrochemical measurements. The lamp gave out directional light with uniform intensity distribution. The light was filtered to simulate the solar spectrum before illuminating the sample. A water filter (Supporting Information, Figure S9) between the lamp and electrochemical cell was used for eliminating the long-wave part of the

radiation during the photocurrent measurement. It also reduced heating of the sample and the electrolyte, caused by the irradiation. The light power illuminating the sample was measured using a Si photodiode as being 270 mW cm^{-2}. During the photocatalytic oxygen-evolution reaction, the amperometric $I–t$ data were acquired from the electrochemical cell. The applied voltage was fixed at 0.22 V (versus Ag/AgCl).

Oxygen Measurement: The oxygen measurement was conducted in a manner similar to the photocurrent measurement. Before the measurement, the anode was purged with highly pure N$_2$ (99.9995%). When the electrode was irradiated, the chromoampometric test was begun at +0.22 V vs. reversible hydrogen electrode (Ag/AgCl) (RHE) for 150 min with O$_2$ bubbling on the anode. 0.8 mL gas was taken from the headspace of the photoanode every 30 min and injected into a gas chromatography machine (Shimadzu GC-8A, Ar carrier gas) to determine the O$_2$ concentration. This was then correlated to the total amount of O$_2$ in the headspace. The amount of O$_2$ in the solution was corrected using Henry's Law.

Supporting Information

Supporting Information is available from the Wiley Online Library or from the author.

Acknowledgements

[1] N. S. Lewis, D. G. Nocera, *Proc. Natl. Acad. Sci. USA* **2006**, *103*, 15729.

[2] M. Armand, J. M. Tarascon, *Nature* **2008**, *451*, 652.

[3] Y. C. Lu, Z. C. Xu, H. A. Gasteiger, S. Chen, K. Hamad-Schifferli, Y. Shao-Horn, *J. Am. Chem. Soc.* **2010**, *132*, 12170.

[4] M. Winter, R. J. Brodd, *Chem. Rev.* **2004**, *104*, 4245.

[5] J. Suntivich, K. J. May, H. A. Gasteiger, J. B. Goodenough, S. H. Yang, *Science* **2011**, *334*, 1383.

[6] Y. Y. Liang, Y. G. Li, H. L. Wang, J. G. Zhou, J. Wang, T. Regier, H. J. Dai, *Nat. Mater.* **2011**, *10*, 780.

[7] A. J. Bard, M. A. Fox, *Acc. Chem. Res.* **1995**, *28*, 141.

[8] M. W. Kanan, D. G. Nocera, *Science* **2008**, *321*, 1072.

[9] R. Eisenberg, *Science* **2009**, *324*, 44.

[10] P. D. Yang, *Nature* **2011**, *482*, 41.

[11] K. B. Zhou, Y. D. Li, *Angew. Chem. Int. Ed.* **2011**, *50*, 2.

[12] W. C. Huang, L. M. Lyu, Y. C. Yang, M. H. Huang, *J. Am. Chem. Soc.* **2011**, *134*, 1261.

[13] A. Paracchino, V. Laporte, K. Siuvla, M. Gratzel, E. Thimsen, *Nat. Mater.* **2011**, *10*, 456.

[14] R. Subbaraman, D. Tripkovic, D. Strmcnik, K. C. Chang, M. Uchimura, A. P. Paulikas, V. Stamenkovic, N. M. Markovic, *Science* **2011**, *334*, 1256.

[15] A. Walsh, J. L. F. Da Silva, S. H. Wei, C. Korber, A. Klein, L. F. J. Piper, A. DeMasi, K. E. Smith, G. Panaccione, P. Torelli, D. J. Payne, A. Bourlange, R. G. Egdell, *Phys. Rev. Lett.* **2008**, *100*, 167402.

[16] J. B. Mu, C. L. Shao, Z. C. Guo, M. Y. Zhang, Z. Y. Zhang, P. Zhang, B. Chen, Y. C. Liu, *J. Mater. Chem.* **2012**, *22*, 1786.

[17] P. Nguyen, H. T. Ng, T. Yamada, M. K. Smith, J. Li, J. Han, M. Meyyappan, *Nano Lett.* **2004**, *4*, 651.

[18] G. Z. Shen, B. Liang, X. F. Wang, H. T. Huang, D. Chen, Z. L. Wang, *ACS Nano* **2011**, *5*, 6148.

[19] H. Xu, R. Q. Zhang, A. M. C. Ng, A. B. Djurisic, H. T. Chan, W. K. Chan, S. T. Tong, *J. Phys. Chem. C* **2011**, *115*, 19710 and references therein.

[20] Z. K. Zheng, B. B. Huang, Z. Y. Wang, M. Guo, X. Y. Qin, X. Y. Zhang, P. Wang, Y. Dai, *J. Phys. Chem. C* **2009**, *113*, 14448.

[21] J. Y. Ho, M. H. Huang, *J. Phys. Chem. C* **2009**, *113*, 14159.

[22] J. Y. Ho, M. H. Huang, *J. Phys. Chem. C* **2009**, *113*, 14159.

[23] M. Epifani, P. Siciliano, A. Gurlo, N. Barsan, U. Weimar, *J. Am. Chem. Soc.* **2004**, *126*, 4078.

[24] C. H. Lee, M. Kim, T. Kim, A. Kim, J. Paek, J. W. Lee, S. Y. Choi, K. Kim, J. B. Park, K. Lee, *J. Am. Chem. Soc.* **2006**, *128*, 9326.

[25] J. Y. Lao, J. Y. Huang, D. Z. Wang, D. Z. Ren, *Adv. Mater.* **2004**, *16*, 65.

[26] Y. F. Li, Z. P. Liu, *J. Am. Chem. Soc.* **2011**, *133*, 15743.

[27] Y. H. Fang, Z. P. Liu, *J. Am. Chem. Soc.* **2010**, *132*, 18214.

[28] G. Cicero, A. Catellani, G. Galli, *Phys. Rev. Lett.* **2004**, *93*, 016102.

[29] Y. F. Li, Z. P. Liu, L. L. Liu, W. G. Gao, *J. Am. Chem. Soc.* **2010**, *132*, 13008.

[30] K. Maeda, M. Higashi, D. Lu, R. Abe, K. Domen, *J. Am. Chem. Soc.* **2010**, *132*, 5858.

[31] B. S. Yeo, A. T. Bell, *J. Am. Chem. Soc.* **2011**, *133*, 5587.

[32] Y. D. Hou, B. L. Abrams, P. C. K. Vesborg, M. E. Bjorketun, K. Herbst, L. Bech, A. M. Setti, C. D. Damsgaard, T. Pedersen, O. Hansen, J. Rossmeisl, S. Dahl, J. K. Norskov, I. Chorkendorff, *Nat. Mater.* **2011**, *10*, 434.

[33] S. Y. Reece, J. A. Hamel, K. Sung, T. D. Jarvi, A. J. Esswein, J. J. H. Pijoers, D. G. Nocera, *Science* **2011**, *334*, 645.

ADVANCED MATERIALS

Supporting Information

Enhanced Photocatalytic Oxygen Evolution by Crystal Cutting

Min Sun, Shijie Xiong, Xinglong Wu, Chengyu He, Tinghui Li, and Paul K. Chu**

Supplementary Information

Enhanced Photocatalytic Oxygen Evolution by Crystal Cutting

By Min Sun, Shijie Xiong, Xinglong Wu, Chengyu He, Tinghui Li and Paul K. Chu

Theoretical calculation details for electron and hole distributions

In order to investigate the distributions of the photoexcited electrons and holes on the {100} and {111} facets of crystal In_2O_3, a first-principle study is conducted on the electronic structure of the bulk In_2O_3 and In_2O_3 films with surfaces along the {100} and {111} directions. The calculation is performed using the generalized gradient approximation (GGA) of the Perdew, Burke, and Ernzerholf (PBE) form[S1] under package CASTEP[S2] in which a plane-wave norm-conserving pseudopotential method[S3] is used. A kinetic energy cutoff of 500 eV is adopted to represent the single-particle wave functions. Slabs are utilized to investigate the band structure and wave functions of the {100} and {111} surfaces of In_2O_3. To form a periodic lattice, the slabs with a thickness of 1.5 nm are stacked periodically and separated by vacuum slabs with a thickness of 1.2 nm. The size of a supercell along the directions of the surface is that of the crystal cell in the plane. The geometry of the configuration is optimized using the BFGS minimizer in the CASTEP package with default convergence tolerances: 2×10^{-5} eV for energy change, 0.5 eV/nm for maximum force, and 2×10^{-4} nm for maximum displacement[S4]. After geometric optimization, the band structure and orbitals of the electrons are calculated using the CASTEP package. As a comparison, the band structure of the In_2O_3 crystal is also derived using the same method after the same geometric optimization. Fig. S1 shows a gap of 1.178 eV at the Γ point, which is larger than

0.93 eV from GGA and smaller than 1.83 eV from GGA+U+SOC obtained with the VASP package[S5]. The calculated gap value is smaller than the experimental one (2.8 eV) due to the well-known systematic underestimation of the gap in the density functional theory. The calculated DOSs for bulk, {100} surface, and {111} surfaces of In_2O_3 are displayed in the main panel of Fig. S4. The spatial distributions of the orbitals at the subband near the top of the valence band created by the {100} surface and at conduction bands of the {100} and {111} slabs are also calculated and shown in the insets of Figs. S2, S3, and S4, respectively. The holes excited from the valence subband are located on the {100} facets while the electrons from the conduction band are extended to the whole system.

In order to investigate the effects of adsorbed H_2O molecules and the change of slab thickness on the band structure, Figs. S5 and S6 plot the DOSs for systems with and without H_2O molecules and for slabs of different thicknesses, respectively. It can be seen that although there are some changes in the detailed structures, peak A with the orbital on the {100} surface still exists thus supporting our analysis.

References

[S1] J. P. Perdew, K. Burke, M. Ernzerhof, *Phys. Rev. Lett.* **1996**, 77, 3865.

[S2] S. J. Clark, M. D. Segall, C. J. Pickard, P. J. Hasnip, M. J. Probert, K. Refson, M. C. Payne, *Zeitschrift fuer Kristallographie* **2005**, 220, 567.

[S3] D. R. Hamann, M. Schluter, C. Chiang, ***Phys. Rev. Lett.*** 1979, 43, 1494.

[S4] B. G. Pfrommer, M. Cote, S. G. Louie, M. L. Cohen, *J. Comput. Phys.* **1997**, 131, 233.

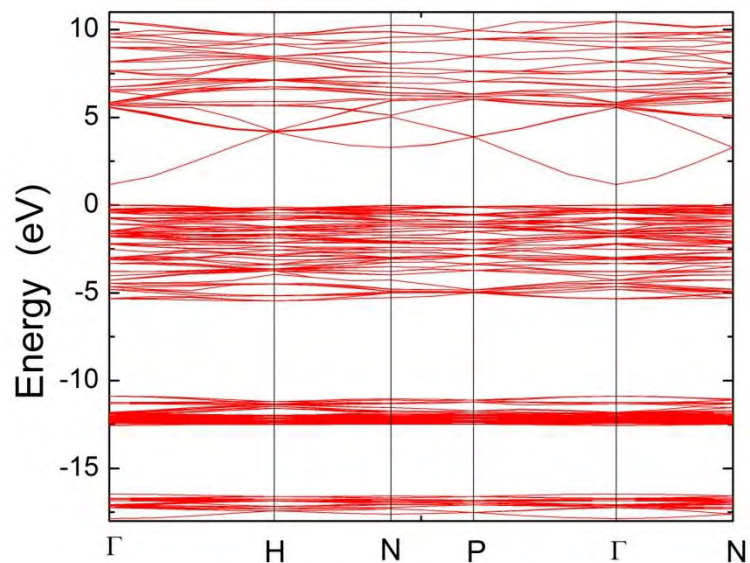[S5] P. Erhart, A. Klein, R. G. Egdell, K. Albe, *Phys. Rev. B* 2007, 75, 153205.

Figure S1. Band structure of bulk In_2O_3 calculated after geometry optimization using the GGA of CASTEP package.
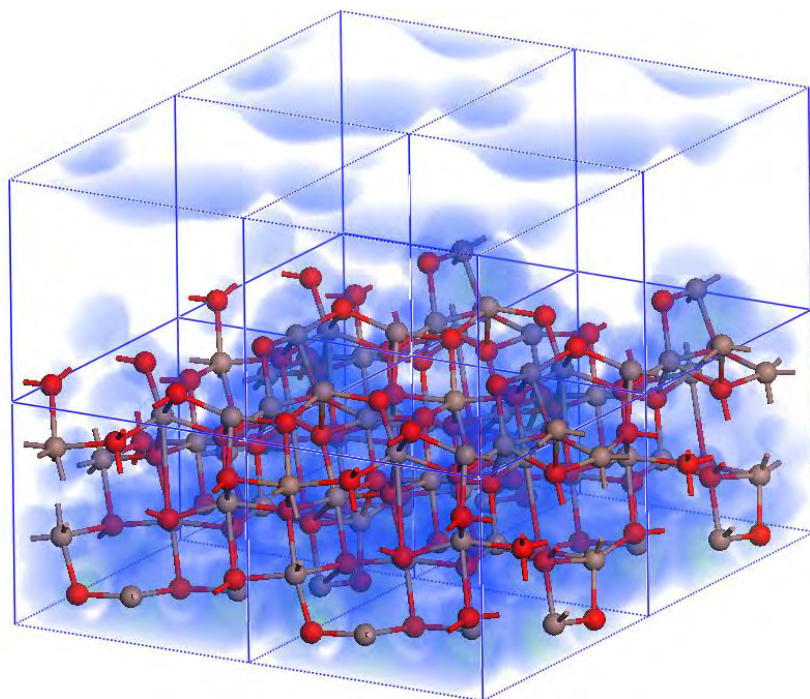
Figure S2. Spatial distribution of the electron orbital at the conduction subband of the {100} slab of In_2O_3. The orbital is extended to the whole materials. The grey and red balls represent In and O atoms, respectively.
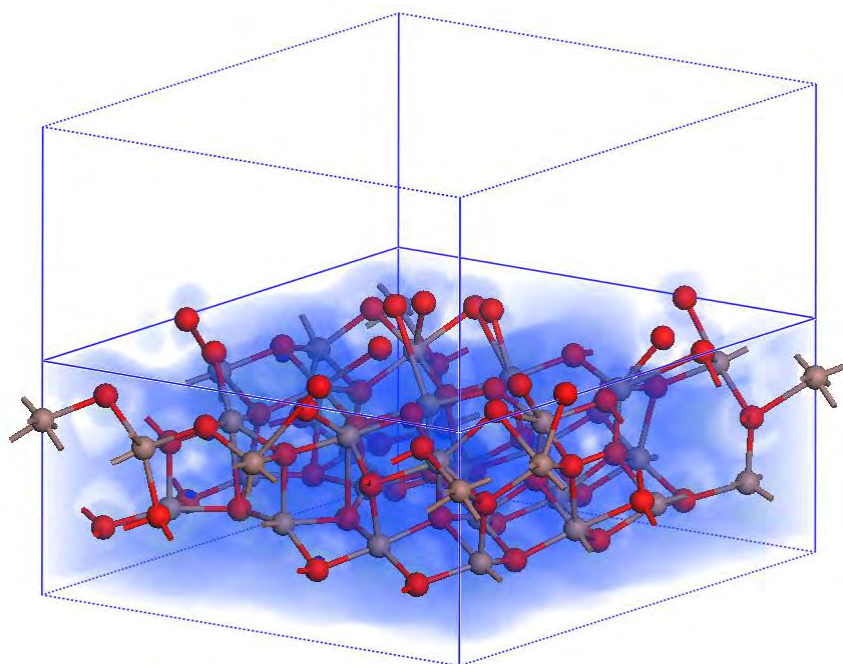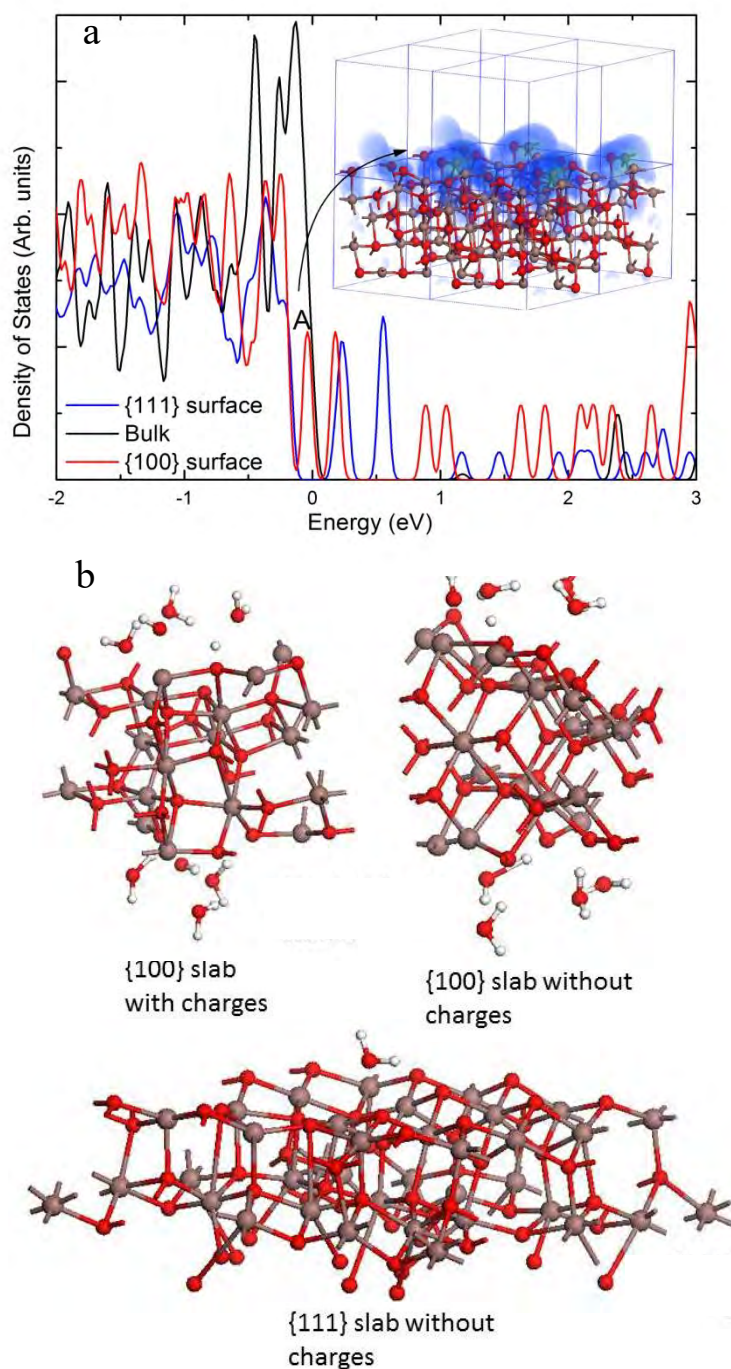
Figure S3. Spatial distribution of electron orbital at conduction subband of the {111} slab of In$_2$O$_3$. The orbital is extended to the whole materials. The grey and red balls represent In and O atoms, respectively.

Figure S4. (a) Densities of states of the bulk and slabs along the {100} and {111} directions of In$_2$O$_3$ (main panel). The inset shows spatial distribution of the orbital at valence subband A of the {100} slab. The grey and red balls represent In and O atoms, respectively. (b) Optimized structures of {100} and {111} slabs with adsorbed H$_2$O molecules. In the case with charges, the bias induced charge is +3e per supercell.
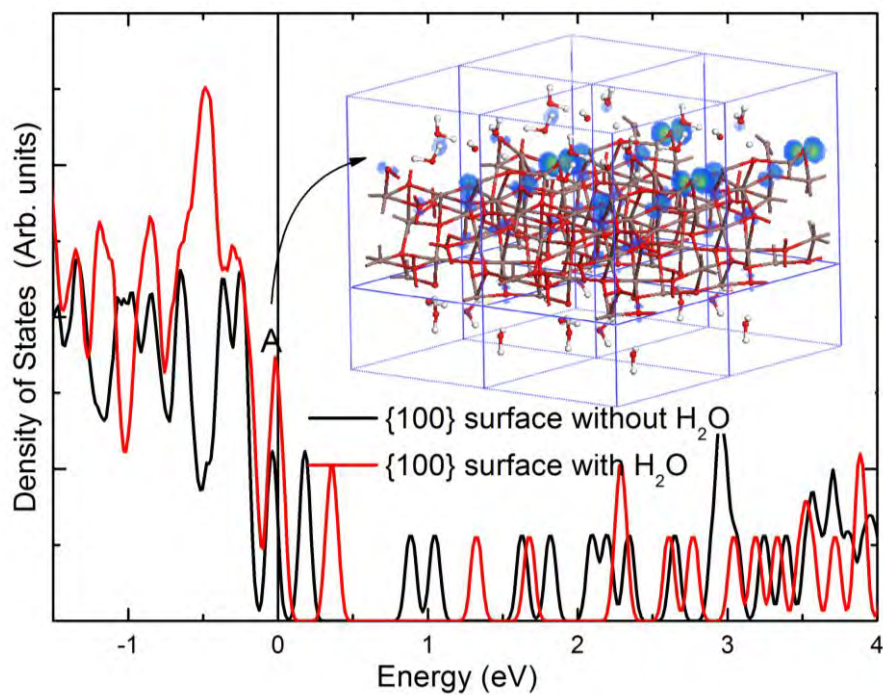
Figure S5. Densities of states of the {100} slabs with and without H_2O molecules (main panel). The inset shows spatial distribution of the orbital at subband A in the case with H_2O molecules. The band calculation in the case with H_2O is based on the structure of the second panel in Fig. 2b.
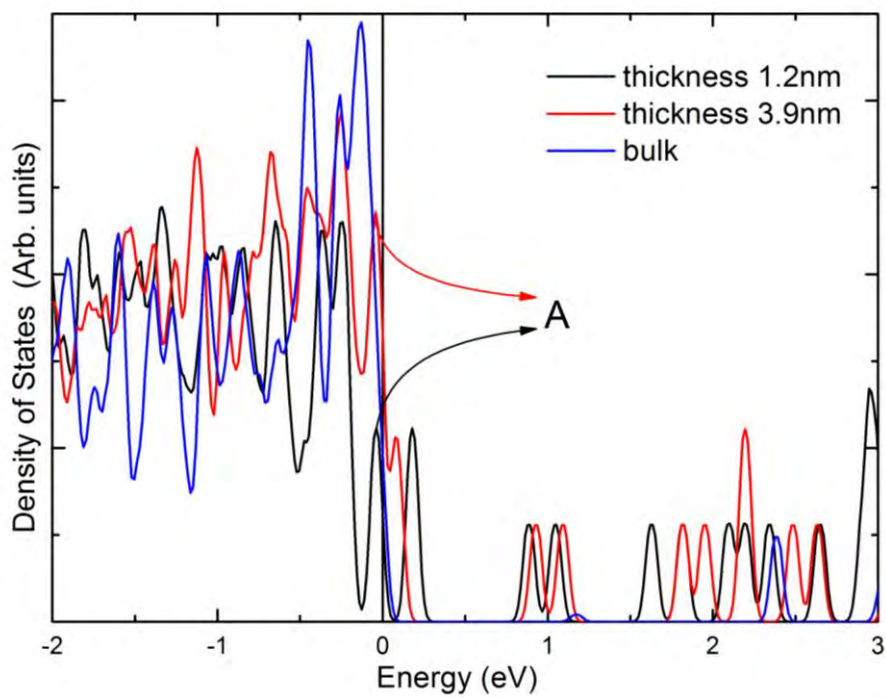
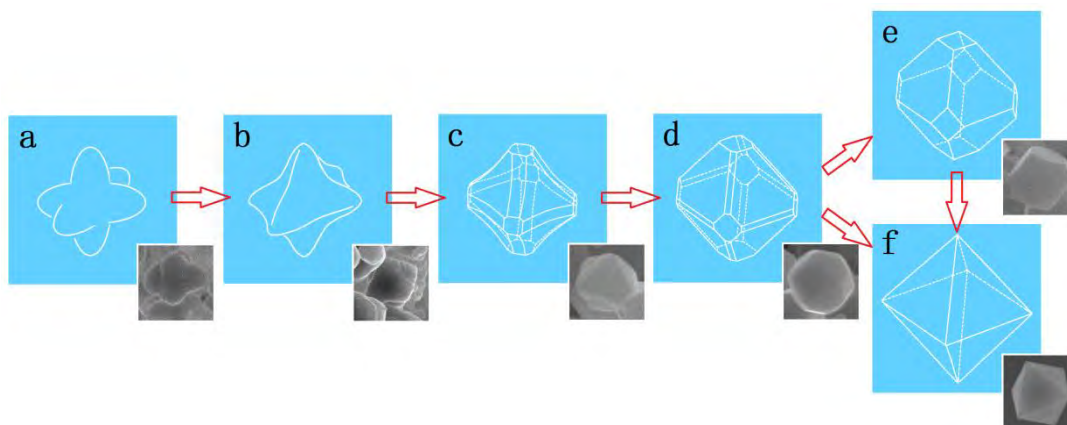Figure S6. Densities of states of the {100} slabs of different thicknesses.

Figure S7. In$_2$O$_3$ nanocrystal nucleation and growth process. (a) Beginning of nucleation (850 ^{o}C) when a three-dimensional structure of indium oxide with six protruberances is first formed. (b) As the temperature rises, the three-dimensional structure begins to take shape. (c) Three basic types of crystal facets emerge at 900 ^{o}C and they are the {100}, {110} and {111} facets. (d) The crystal surface becomes smoother at 900-950 ^{o}C. (e-f) Truncated octahedrons and octahedrons with a uniform size deposited at 950 and 1000 ^{o}C at a gas flow of 150 and 100 sccm for 3 h, respectively.
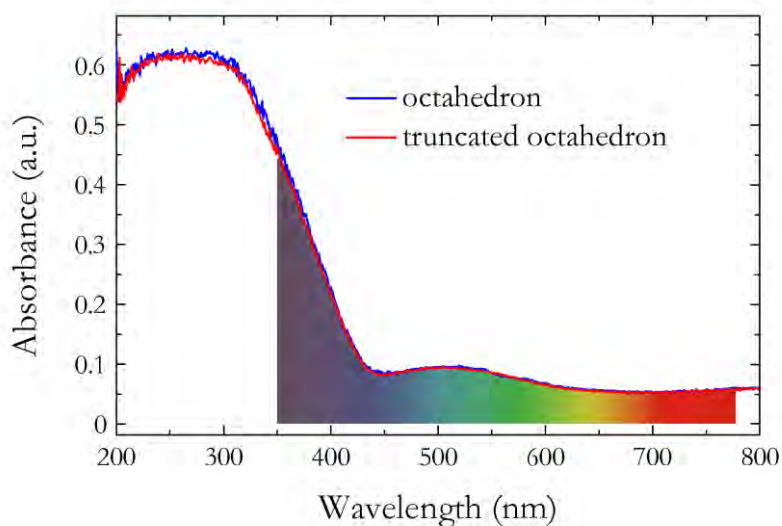
Figure S8. Calculated Kubelka-Munk function versus wavelength in the range of 200 to 800 nm for the octahedron and truncated octahedron samples (absorption spectra). The visible region is indicated as a color area. They are obtained from the ultraviolet–visible diffusive reflectance spectra taken using the diffuse reflection method on a VARIAN Cary5000 spectrophotometer. The two curves are identical, indicating that no absorption change occurs for the two kinds of In_2O_3 octahedrons.
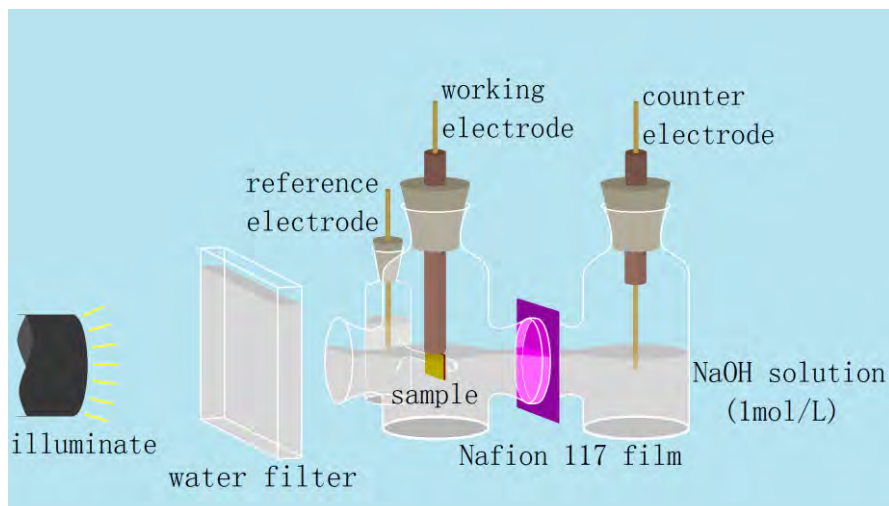
Figure S9. Schematic of the electrochemical cell composed of three chambers. The anode and cathode electrodes are immersed in separate cells divided by a Nafion 117 film and a Luggin capillary separates the working compartment from the reference compartment. A Ag/AgCl electrode in 1 mol/L NaOH solution (with a nominal potential of 0.210 V versus reversible hydrogen electrode) and a platinum wire are used as the reference and counter electrodes, respectively. The working electrode is a 0.8 cm x 1.2 cm silicon substrate modified with the In_2O_3 catalysts. Typically, a 0.8 cm x 0.8 cm substrate is immersed in the solution. The electrolyte is purged with N_2 for 30 min to eliminate dissolved gases such as O_2 before the measurement and a 500 W Xe lamp serves as the light source in the photoelectrochemical measurements. A water filter lying between the lamp and electrochemical cell was used for filtering out the long-wave part of the radiation during photocurrent measurement.

Figure S10. Enlarged digital photograph showing oxygen evolution from the truncated In$_2$O$_3$ octahedral electrodes taken at 60 min (amperometric $I - t$ curves).
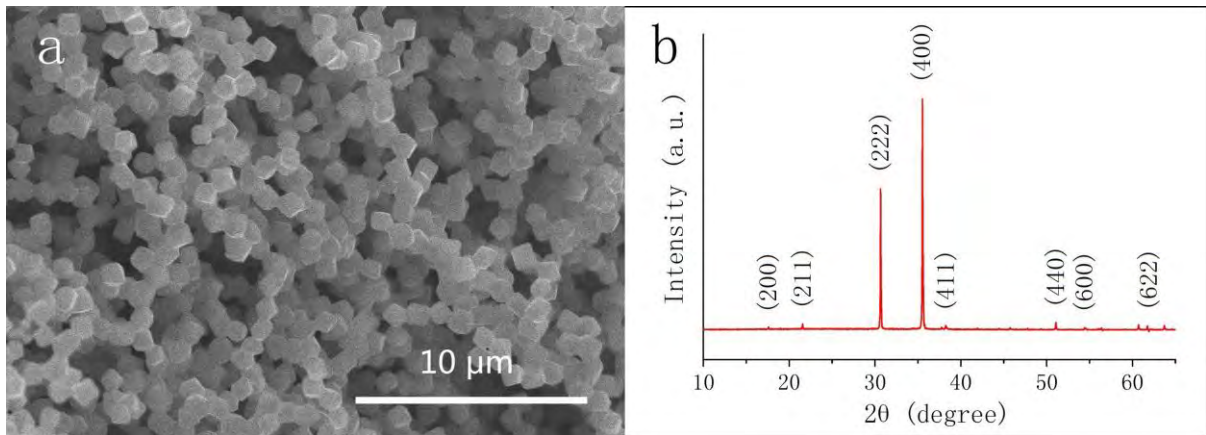
Figure S11. (a) Low-magnification FE-SEM image and (b) XRD spectrum of the truncated octahedron In_2O_3 obtained after photoelectrochemical experiment. These results confirm that the truncated octahedrons remain intact on the substrate.